Journal of Materials Science & Technology 204 (2025) 18–28

Contents lists available at ScienceDirect

Journal of Materials Science & Technology

journal homepage: www.elsevier.com/locate/jmst

Research Article

A universal strategy to synthesize amorphous/crystalline P, Mo dual-doped CoNiS nanostructures for overall water splitting

Xiaodong Yang, Haochen Shen, Xiaoming Xiao, Wei Yang, Zhichao Li, Na Yang, Luhong Zhang*

School of Chemical Engineering and Technology, Tianjin University, Tianjin 300072, China

ARTICLE INFO

Article history:
Received 21 October 2023
Revised 30 November 2023
Accepted 22 February 2024
Available online 16 April 2024

Keywords:
Transition metal sulfides
Dual doping
Amorphous/crystalline hybrid
Water splitting

ABSTRACT

In this work, P and Mo dual-doped CoNiS (PMo-CoNiS) nanosheet arrays were successfully constructed through a common solvothermal treatment. The precise doping of P and Mo species into the CoNiS can regulate the microstructures and meanwhile endow with PMo-CoNiS abundant amorphous/crystalline heterointerfaces, which can adjust the electronic structure, thus enhancing the intrinsic activity of hydrogen evolution reaction (HER) and oxygen evolution reaction (OER). As a result, ultra-low overpotentials of merely 156 and 58 mV are required to deliver a current density of 10 mA cm^{-2} for OER and HER, respectively, and the electrocatalysts PMo-CoNiS also exhibit low Tafel slopes and maintain robust stability for 48 h in alkaline media at a high current density of 50 mA cm^{-2}. In addition, in an assembled electrolyte cell for overall water splitting, a voltage as low as 1.48 V is sufficient to yield a current density of 10 mA cm^{-2}. Density functional theory (DFT) calculations further confirmed that the enhanced OER and HER result from the optimized OH^* and H^* adsorption energy of PMo-CoNiS due to P, Mo dual doping and generated interfacial effect. This work may offer an avenue for designing low-cost bifunctional catalysts with superior catalytic activity and provide a new application strategy for broader applications in various electrocatalytic fields.

1. Introduction

Electrochemical water splitting is widely considered an economically viable and environmentally friendly technique to generate hydrogen energy for addressing issues related to environmental pollution and the fossil energy crisis [1,2]. It involves two half-reactions: the hydrogen evolution reaction (HER) at the cathode and the oxygen evolution reaction (OER) at the anode [3,4]. Nevertheless, the utilization of state-of-the-art Pt-based and Ir/Ru-based commercialized catalysts for HER and OER is severely hindered by limitations such as high cost, scarcity, and poor stability. Additionally, using identical anode and cathode materials in a single water-splitting apparatus has been suggested to enhance efficiency due to improved compatibility [5]. Therefore, developing efficient, low-cost, and stable bifunctional electrocatalysts for water splitting has emerged as a focal point of research to promote large-scale industrial applications for water splitting.

Within this context, due to features of low cost and earth abundance, various transition metal-based materials, including carbides [6,7], phosphides [8,9], sulfides [10,11], and hydroxides [12,13], have been served as OER, and HER bifunctional electrocatalysts in alkaline media for a long time. Among these, transition metal sulfides (TMSs), such as Ni_2S_3 [14,15], Co_3S_4 [16,17], and MoS_2 [18,19], are widely used as non-noble metal alternatives due to their fascinating electrochemical properties. However, limitations concerning deficient active sites and low conductivity greatly restrict the activity of TMSs for water splitting. Fortunately, interface engineering and heteroatom doping engineering have been identified as viable strategies for obtaining fine-tuning electronic structures and improving unsatisfactory catalytic performance [11,20]. Specifically, engineering multiphase compounds can rearrange the electron on the heterogeneous interfaces and expose additional active sites, thereby outperforming single-component catalysts [21,22]. In these hybrid amorphous/crystalline nanostructures, the advantages of superior conductivity from the crystalline phase and sufficient active sites from the amorphous phase are synergistically integrated, thus efficiently optimizing the electronic structure and commendably realizing the goal of good activity and stability towards both OER and HER [23]. The routine fabricated techniques include the electrochemical method [24], chemical etching [25], pyrolysis method [26], etc. For example, Xu and co-workers [27] reported the amorphous/crystalline heterostructure (CoMP/CoM LDH) with

* Corresponding author.
E-mail address: zhanglvh@tju.edu.cn (L. Zhang).

https://doi.org/10.1016/j.jmst.2024.02.082
1005-0302/

increased catalytic active sites and more optimal intermediate adsorption/dissociation capability through a thermal pyrolysis route. Likewise, a two-step ion exchange and spontaneous redox reaction approach was implemented by our group to develop crystalline Ag nanoparticles on amorphous quaternary LDHs (Ag/QLDHs), demonstrating enhanced catalytic activity and stability for OER [28].

Notably, the doping strategy is also critically recognized for its ability to tune the d-band center and enhance the performance of electrocatalysts. The subtle lattice distortion and vacancy caused by the incorporation of a single heteroatom into the lattice can modulate the electronic structure at the atomic level [29,30]. For instance, Xu and co-workers [31] developed a P-doping strategy to synthesize phosphorus-doped monoclinic β-$CoMoO_4$ (P-$CoMoO_4$) microarrays with enhanced HER and OER performance due to creating more active sites. Furthermore, simultaneous doping of two kinds of two foreign atoms is an effective strategy to strengthen the regulation of the electronic structure. For example, Peng et al. [32] reported a Fe- and Ni-codoped CoS_2, which demonstrated significantly improved OER activity and robust stability in an alkaline medium due to the synergistic effects of Fe and Ni atoms. However, to the best of our knowledge, the dual-heteroatom doping strategy is rarely reported to construct amorphous/crystalline heterostructures, which can become the “one stone, two birds” design to coordinatively regulate the electronic interaction, and is greatly expected to improve overall water-splitting activity and stability.

Recently, introducing the non-3d high-valence metals (Mo, W, etc.) into 3d metals has been identified as a highly efficient doping means in optimized Gibbs free energy of reaction intermediates [33,34]. Taking the above as inspiration, a universal method was employed to design and construct Mo-doped CoNiS heterostructures with trace P modifications, yielding a novel bifunctional electrocatalyst of water splitting (PMo-CoNiS). The generated amorphous/crystalline heterostructures, regulated by dual-doped P, Mo, facilitated exposing active sites and optimizing adsorption energies, thereby boosting the catalytic activity towards both HER and OER. As expected, the fabricated PMo-CoNiS exhibits an ultralow overpotential of 156 mV for OER and 58 mV for HER at 10 mA cm^{-2}. Besides, the water-splitting cell only needs a low voltage of 1.48 V to deliver a current density of 10 mA cm^{-2}. In addition, the catalyst also demonstrated robust long-term durability, maintaining its activity for 48 h under 50 mA cm^{-2} in a 1 M KOH solution. Density functional theory (DFT) calculations attested that the P, Mo dual doping effectively modulates the charge transfer, optimizes the adsorption/desorption behavior of the electrocatalyst for H* and OH*, and consequently lowers the Gibbs free energy. This work provides a universal dual-doping strategy for constructing heterogeneous amorphous/crystalline nanostructures toward water-splitting, offering a promising route for further research in this and other related fields.

2. Experimental section

2.1. Chemicals

2-Methylimidazole ($C_4H_6N_2$, AR) was purchased from Shanghai Macklin Biochemical Co., Ltd. (Shanghai, China). Thioacetamide (CH_3CSNH_2, AR), nickel sulfate heptahydrate ($NiSO_4{\cdot}7H_2O$, 99%), phosphotungstic acid ($H_3[P(W_3O_{10})_4]{\cdot}xH_2O$, AR), and phosphomolybdic acid ($H_3[P(Mo_3O_{10})_4]{\cdot}xH_2O$, AR) were purchased from Tianjin Heowns Biochem LLC (Tianjin, China). Cobaltous nitrate hexahydrate ($Co(NO_3)_2{\cdot}6H_2O$) was supplied by Shanghai Aladdin Bio-Chem Technology Co., Ltd. (Shanghai, China). The nickel foam (N.F., thickness: 1.6 mm) was obtained from the Tenterhook Electronic Technology Co., Ltd. (Kunshan, China). Deionized water (> 18.2 MΩ) was used in all experiments. All chemicals were used without further purification.

2.2. Synthesis of catalysts

2.2.1. Preparation of Co ZIF

First, Ni foam was purified by sonicated in HCl (1 M), deionized water, and ethanol for 15 min to remove the surface impurities and then dried out overnight at 60 °C. After that, $Co(NO_3)_2{\cdot}6H_2O$ (0.58 g) and 2-methylimidazole (1.34 g) were dissolved in 40 mL water, separately, and stirred for 10 min. These solutions were combined and stirred for an additional 30 min. Then, the treated NF was immersed and kept for 4 h. The as-prepared foam was washed with water and ethanol several times to remove the residual 2-Methylimidazole on its surface.

2.2.2. Preparation of CoNi LDH

Typically, a piece of as-prepared Co zeolitic imidazolate frameworks (ZIF) was immersed into the 15 mL water solution with 0.05 g $NiSO_4{\cdot}7H_2O$ and 0.05 g $Co(NO_3)_2{\cdot}6H_2O$ in a 20 mL glass bottle and then placed in an oven and maintained at 70 °C for 1 h. Subsequently, the bottle was taken out and cooled down to room temperature, and the CoNi nanosheets were obtained through multiple washings with deionized water and ethanol, followed by overnight drying at 60 °C.

2.2.3. Preparation of CoNiS, Mo-CoNiS, PMo-CoNiS, and PW-CoNiS

We chose a solvothermal method to fabricate a series of sulfides. Specifically, 5 mmol of thioacetamide (TAA) was dissolved in 40 mL ethanol and stirred for 15 min by a magnetic stirrer to form a homogeneous solution. The obtained solution was then transferred into a 50 mL Teflon-lined stainless-steel autoclave containing a piece of processed CoNi LDH and maintained at 120 °C for 6 h. After the reaction, the resulting CoNiS product was washed with deionized water and ethanol before drying overnight at 60 °C. In addition, the synthesis of Mo-CoNiS, PMo-CoNiS, and PW-CoNiS was kept under the same conditions, with the exception that specified amounts of Na_2MoO_4, phosphomolybdic acid (PMo), or phosphotungstic acid (PW) were added.

2.2.4. Preparation of commercial RuO_2/NF and Pt/C/NF

30.0 μL Nafion solution (5 wt.%), 900.0 μL absolute ethanol, and 10.0 mg commercial RuO_2 or Pt/C powder were sonicated for 2 h to prepare the RuO_2 ink solution. Then the proper amount of ink was transferred onto the NF to fabricate RuO_2 supported on the NF electrode (RuO_2 or Pt/C).

2.3. Materials characterization

The fabricated electrocatalysts were characterized by scanning electron microscopy (SEM, S-4800, Hitachi) and high-resolution transmission electron microscopy (HRTEM, JEM-F200, Hitachi) equipped with energy dispersive spectroscopy (EDS). X-ray diffraction (XRD) patterns were recorded by a powder X-ray diffractometer (D8-Focus, Bruker) with Cu $K\alpha$ radiation (λ = 1.5406 Å) at a scan rate of 6°/min. X-ray photoelectron spectroscopy (XPS) analysis was conducted on a Thermo Fisher Scientific to analyze the elemental composition and chemical environments.

2.4. Electrochemical measurements

The electrochemical performances were conducted by a typical three-electrode configuration using an electrochemical workstation (CHI 760, Shanghai). Specifically, the fabricated catalysts were used as the working electrode, while the Hg/HgO electrode and graphite rod were employed as the reference and counter electrode, respectively. Linear sweep voltammetry (LSV) tests were conducted at the scan rate of 5 mV s^{-1} in a 1.0 M KOH solution with a 90%

iR compensation. Electrochemical surface areas (ECSA) were determined based on the electrochemical double capacitance (C_{dl}) using a CV method in a non-Faradaic potential range at various scan rates (20–120 mV s^{-1}). Electrochemical impedance spectroscopy (EIS) assessments were performed on the same three electrodes in a 1 M KOH electrolyte, with a frequency range of 0.01–10^5 Hz and an amplitude of 10 mV. Stability measurements were performed by *i–t* test. According to the Nernst equation, all the potentials reported here were referenced to a reversible hydrogen electrode ($E_{RHE} = E_{Hg/HgO} + 0.059\ pH + 0.197$).

3. Results and discussion

3.1. Material synthesis and characterization

The synthetic route of the PMo-CoNiS is schematically illustrated in Fig. 1. Firstly, Co ZIF nanoarrays were vertically grown on the Ni foam substrate according to a wet chemical method at room temperature. Subsequently, the ion-exchange reaction occurred after Co ZIF was immersed in the mixed solution of $NiSO_4{\cdot}7H_2O$ and $Co(NO_3)_3{\cdot}6H_2O$. In this process, the ZIF arrays served as a self-sacrificial template to generate the Co LDH nanosheets on its skeleton, in which the organic ligand 2-methylimidazole, originally on the surface of ZIF precursor, was removed, and Co^{2+} ions were replaced by encountered Ni^{2+} ions in the solution. Afterward, the final PMo-CoNiS products were obtained through a solvothermal method conducted at 120 °C. TAA and PMo served as sources for S, Mo, and trace P, respectively. Consequently, this process can achieve the dual-doping heterostructures PMo-CoNiS. The morphology and microstructures of samples were characterized by scanning electron microscope (SEM) and transmission electron microscope (TEM). SEM images (Fig. S1 in the Supplementary Material) reveal that the Co ZIF precursors synthesized uniform-sized arrays with smooth surfaces on the Ni foam substrate. Subsequently, after introducing the Co^{2+} and Ni^{2+} sources, an ideal nanosheet array structure was formed on the ZIF surface (Fig. S2). However, the solvothermal sulfurization reaction partly changed the morphology, in which the surface became rough, and some large nanoparticles were generated on their surface when a certain amount of PMo was added, as exhibited in Fig. 2(b). Notably, this unique structure is markedly different from the morphology of pure CoNiS as shown in Fig. 2(a). The TEM images in Figs. 2(c) and Fig. S3 further confirmed the internal structure evolution. In the HRTEM images presented in Fig. S3, the subtle lattice fringes belonging to LDH could be observed. After the sulfurization reaction with PMo, the morphology greatly changed, as shown in Fig. 2(c). The corresponding HRTEM and inverse fast Fourier transform (IFFT) reveal that the interplanar distances of 0.283 nm are consistent with the (311) planes of Co_3S_4, and the lattice spacing of 0.182 nm corresponds to the (211) plane of Ni_3S_2, indicating the coexistence of both in the nanostructures. Moreover, the EDS element mapping images (Fig. 2(d–i)) evidenced the homogeneous distribution of Ni, Co, S, Mo, and P elements throughout the nanosheet structure. The concentrations of P, Mo, Co, Ni, and S in the PMo-CoNiS were determined by inductively coupled plasma-atomic emission spectrometry (ICP-AES). It shows the atom ratio of them is 0.08, 4,64, 44.87, 35.16, and 12.25, respectively, which has a similar result to XPS (Table S1).

To explore the evolution process of nanostructures and compositions in P, Mo doped-CoNiS, a series of PMo-CoNiSs were synthesized by simply changing the concentration of added PMo ranging from 20 to 160 mg. These variations were denoted as PMo1-CoNiS (20 mg), PMo2-CoNiS (40 mg), PMo-CoNiS (80 mg), and PMo4-CoNiS (160 mg), respectively. As exhibited in Fig. 3(a–d), the morphology of PMo evolved with different doping levels. With the addition of a low amount of PMo, the PMo1-CoNiS still displayed the same nanostructure with plentiful nanosheets on the surface, closely resembling that of the undoped CoNiS sample (Figs. 3(a_1, a_2) and S4). Upon the addition of 40 mg of PMo, we observed the formation of small nanospheres, each with a diameter of about 350 nm, attaching to the surface of the nanosheets, as depicted in Fig. 3(b_1, b_2) (PMo2-CoNiS). Increasing the amount of PMo to 80 mg, large nanospheres of various sizes emerged (Fig. 3(c_1, c_2), PMo-CoNiS). When PMo was added to 160 mg, the number of nanospheres with large sizes on the micron sheets further increased (Fig. 3(d_1, d_2), PMo4-CoNiS). Such a morphology change has not been reported yet and warrants further investigation via TEM to investigate the evolution process further. From the TEM images of PMo1-CoNiS (Fig. 3(a_3, a_4)), the morphology is identical to the undoped CoNiS. Meanwhile, regularly long-range order atoms can be observed on the PMo1-CoNiS nanosheets, and the interplanar spacing of 0.283 and 0.182 nm corresponds to the (311) and (211) planes of CoNiS, respectively. As more PMo are added, the PMo2-CoNiS maintained its primary morphology unchanged but with some tiny nanospheres. Moreover, the amorphous region and defects emerged, as shown in the high-resolution TEM image, indicating the formation of amorphous/crystalline heterogeneous nanostructures (Fig. 3(b_4)). The catalyst PMo2-CoNiS shows a more amorphous region as compared with the PMo1-CoNiS, indicating that increased PMo could generate a more disordered crystal structure [35]. Fig. 2(c_3, c_4) shows that when the Mo content was added to 80 mg, the PMo-CoNiS was almost turned into amorphous structures, retaining only minor crystalline regions. What is more, with further PMo doping, the nanoparticles on the thicker nanosheets

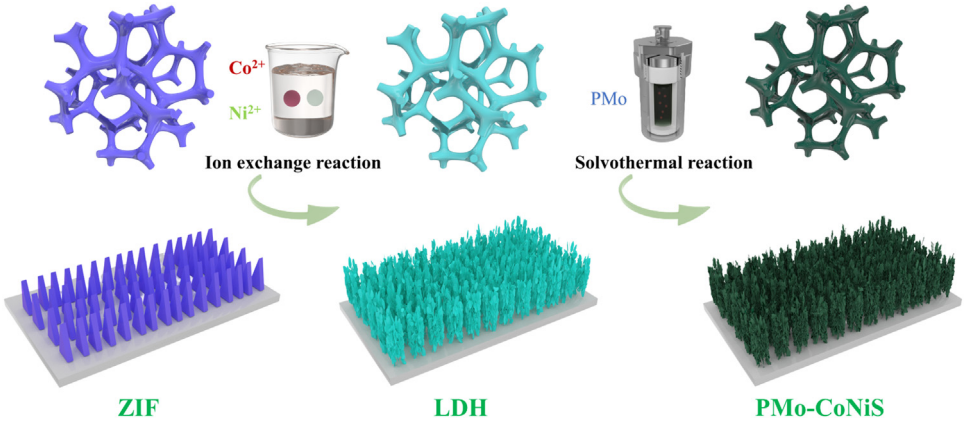

Fig. 1. Schematic illustration of the synthesis of PMo-CoNiS on the Ni foam.

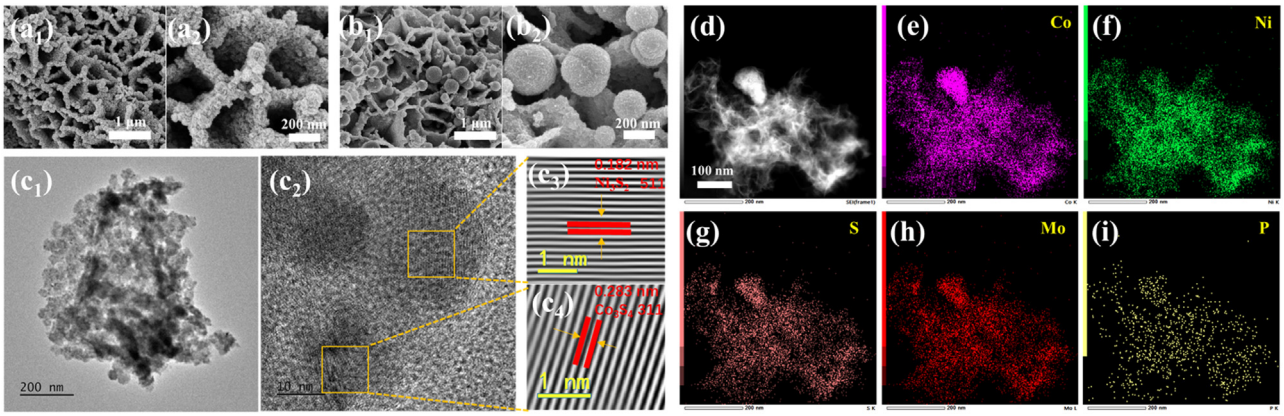

Fig. 2. SEM images of (a) CoNiS, (b) PMo-CoNiS, and (c) TEM, HRTEM images, and IFFT of PMo-CoNiS. (d–i) The elemental color mappings of PMo-CoNiS.

were entirely composed of pure amorphous nanostructures (Fig. 3(d_3, d_4)). Notably, the generated nanoparticles on the nanosheets were always amorphous.

The phase compositions of different as-prepared samples were analyzed by XRD. For the NiCo LDH samples, several small peaks are indexed as the typical LDH structure (JCPDS NO.51-0463) [36], confirming the successful synthesis of NiCo LDH on the Ni foam (Fig. S5). However, the peaks of LDH disappear after the solvothermal reaction, as shown in Fig. 4(a) for the CoNiS sample. It exhibits typical characteristic peaks of Ni_3S_2 (JCPDS NO.44-1418), Co_3S_4 (JCPDS No. 47-0138), and Ni foam. The positions of the two prominent peaks at 50.1° and 55.3° match well with the (211) and (300) crystal planes of Ni_3S_2, respectively [37,38]. Furthermore, the diffraction peaks at 31.5° can be ascribed to (311) crystal planes of Co_3S_4 [39,40]. The above results imply that the LDH was transformed entirely to Co_3S_4 and Ni_3S_2 on the foam surface. When the PMo were added, no extra peaks appeared except the presence of peaks belonging to Co_3S_4, Ni_3S_2, and Ni foam, and results indicate the doping of P and Mo species into the lattice of Co_3S_4/Ni_3S_2. XRD patterns of various P, Mo-doped CoNiS were also conducted to observe the composition changes through the doping effect. As shown in Fig. 4(a), a mixed phase of Co_3S_4/Ni_3S_2 was observed in the case of undoped P, Mo. After adding PMo, the typical diffraction peaks of Co_3S_4/Ni_3S_2 gradually decreased, yet no new diffraction peaks appeared. However, when the PMo was added to 80 mg (PMo-CoNiS), almost all the typical peaks of Co_3S_4/Ni_3S_2 disappeared, leaving only a residual peak at 31.5°. Except for the typical peaks of Ni foam, the PMo4-CoNiS shows a completely amorphous phase according to the XRD analysis, which is consistent with the TEM results. The broadened diffraction peaks and TEM images (Fig. S6) manifest the declined crystallinity of Co_3S_4/Ni_3S_2, indicating the presence of defects in the structures of Co_3S_4/Ni_3S_2, which could provide more active sites and facilitate the OER and HER [41]. By this universal method of manipulating the added amount of PMo with precision, we can fine-tune the extent of conversion, thus adjusting the microstructure and chemical composition of the catalysts. Besides, a series of PW-CoNiS (from PW1-CoNiS to PW3-CoNiS) was also synthesized. XRD, SEM, and TEM analyses (Figs. S7–S10) confirmed that these samples transform akin to those observed in PMo-CoNiS.

XPS measurements were carried out to explore the surface composition and chemical valence states of the constituent elements. As shown in Fig. 4, the XPS spectrum exhibits that the main elements of PMo-CoNiS are Co, Ni, Mo, P, and S, respectively, which follow the EDS mapping results. In the high-resolution Co 2p spectrum (Fig. 4(b)), both the $2p_{1/2}$ and $2p_{3/2}$ were deconvoluted into three peaks. Peaks located at 797.9 and 781.6 eV are assigned to Co^{2+}, while those at 793.1 and 777.4 eV are assigned to Co-S. It can be observed that Co 2p shifted toward the higher binding energy as compared to that of CoNiS, which indicates the electronic structure of Co centers is well modified through P, Mo doping. As for the high-resolution Ni 2p spectrum, the six separated peaks, as displayed in Fig. 4(c), of which the peaks located at 856.2 and 874.1 eV belong to Ni^{2+}, while those centered at 853.2 and 869.7 eV match Ni^0. Significantly, the Ni 2p peaks of PMo-CoNiS exhibit a positive shift of approximately 0.15 eV compared to the peaks of the undoped CoNiS, suggesting the strong electronic interactions by adding PMo. The high-resolution spectrum of the S 2p spectrum in PMo-CoNiS (Fig. 4(d)) can be divided into three peaks. The two apparent peaks of S $2p_{3/2}$ and S $2p_{1/2}$ binding energies are separately divided into two peaks of 161.4 and 162.2 eV, as well as 163.1 and 164.3 eV, indicating the coexistence of S^{2-} and S_2^{2-}. Besides, the peaks at ~168.6 eV manifest the presence of oxidized sulfur (SO_4^{2-}) on the surface of PMo-CoNiS in the open air [42]. Compared with CoNiS, the S 2p peaks for PMo-CoNiS exhibited a negative shift, suggesting the valence state change of S on the surface due to the P, Mo dopant. In the Mo 3d spectrum, as seen in Fig. 4(e), the binding energies at ~229.1 and ~232.3 eV are characteristic of Mo^{4+} $3d_{3/2}$ and Mo^{4+} $3d_{5/2}$, which suggests the successful Mo^{4+} doping in the PMo-CoNiS. An additional peak at 235.4 eV can be ascribed to Mo^{6+} [37]. The presence of an S 2 s peak near the Mo 3d region at 226.2 eV suggests the formation of M-S bonds (M = Co, Ni). In Fig. 4(f), the high-resolution P 2p spectrum shows the two weak peaks, of which binding energies at 128.9 and 130.2 eV are assigned to P $2p_{3/2}$ and P $2p_{1/2}$ respectively, and the peaks located at 133.3 eV match with the P-O bond, demonstrating the existence of trace P in PMo-CoNiS [43]. Compared with CoNiS, the PMo-CoNiS sample exhibited a positive shift in the binding energies of Co $2p_{3/2}$ and Ni $2p_{3/2}$ and a negative shift in S 2p. The binding energies of Co $2p_{3/2}$, and Ni $2p_{3/2}$ exhibit positive shifts, while the S 2p negatively shift, suggesting the strong electronic interactions existed in CoNiS after P and Mo doping resulted in a more positive charge of Co species, Ni species, and negative charge of S species after P and Mo doping [44]. Additionally, the XPS result further proves that P and Mo species have been successfully doped into Ni_3S_2 and Co_3S_4, which can redistribute the electrons at the heterogeneous amorphous/crystalline interfaces, thus enhancing the electrocatalytic performance.

3.2. Electrochemical performances

3.2.1. OER performance

The LSV curves of different samples of PMo-CoNiS for OER were systematically evaluated in a 1.0 M KOH solution using a standard three-electrode system. Remarkably, the PMo-CoNiS shows better OER activity than PMo1-CoNiS, PMo2-CoNiS, and PMo4-CoNiS (Fig.

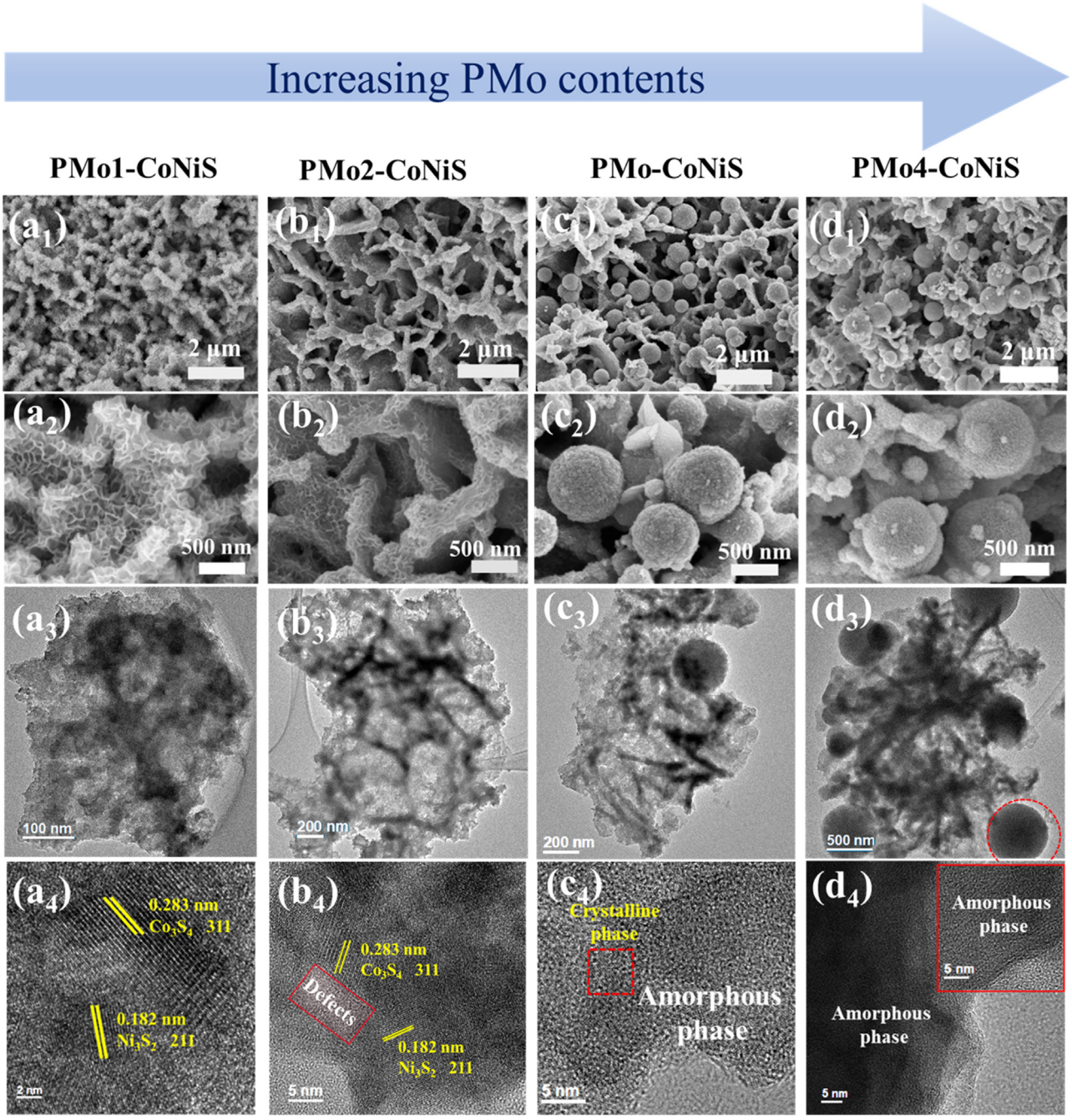

Fig. 3. The structural evolution process from PMo1-CoNiS to PMo4-CoNiS. (a, b) The SEM images and (c, d) TEM images with different magnifications for PMo1-CoNiS, PMo2-CoNiS, PMo-CoNiS, and PMo4-CoNiS.

S11). The data reveal that the electrocatalytic activity of PMo-CoNiS is positively correlated with the amount of PMo within a specific range due to the appropriate ratio of the amorphous/crystalline region, and unique structures. Moreover, the reference samples, including CoNi LDH, CoNiS, Mo-CoNiS, and PW-CoNiS, were also investigated under the same conditions for comparison. As shown in Fig. 5(a), the LSV curves of the PMo-CoNiS exhibit the optimal catalytic activity with the lowest OER overpotentials of 156 and 218 mV to deliver the current densities of 10 and 100 mA cm^{-2}, respectively. While for the CoNi LDH, CoNiS, Mo-CoNiS, and PW-CoNiS catalysts, the overpotentials of 306 (375), 254 (347), 200 (278), and 194 (269) mV are required (Fig. 5(b)). The overpotentials of CoNiS and Mo-CoNiS are larger than those of PMo-CoNiS electrocatalysts, which demonstrates that the synergistic enhancement in OER performance is mediated by P, Mo co-doping. The Tafel slopes of all the electrocatalysts are exhibited in Fig. 5(c), of which PMo-CoNiS has the smallest value of 43.42 mV dec^{-1}, which outperforms that of CoNiS (72.55 mV dec^{-1}), Mo-CoNiS (70.47 mV dec^{-1}), PW-CoNiS (68.75 mV dec^{-1}), and CoNi LDH (74.59 mV dec^{-1}). The lowest overpotential and the smallest Tafel slope manifest that the PMo-CoNiS has excellent electrocatalytic performance and fast kinetics towards OER in the alkaline medium. The enhanced OER activity of PMo-CoNiS could be attributed to the optimal chemical composition and exposure to more active sites by P, Mo dual doping. In addition, the outstanding activity of electrocatalytic PMo-CoNiS is superior to that of most recently reported sulfide-based OER electrocatalysts (Table S2). The fast reaction kinetics can be further revealed by EIS at the constant potential, as

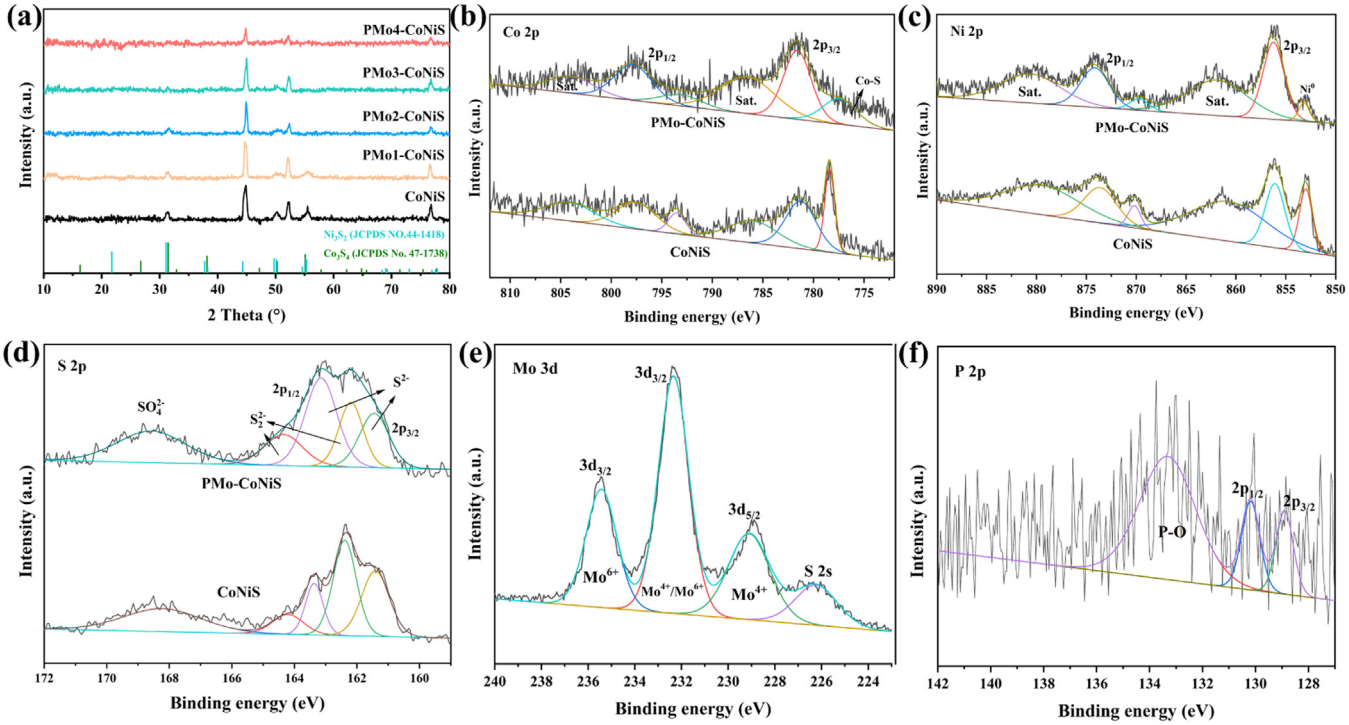

Fig. 4. (a) XRD patterns of CoNiS, PMo1-CoNiS, PMo2-CoNiS, PMo-CoNiS, and PMo4-CoNiS. XPS spectra of (b) Co 2p and (c) Ni 2p, (d) S 2p for PMo-CoNiS. (e) Mo 3d and (f) P 2p spectra for PMo-CoNiS.

shown in Fig. 5(e). The R_{ct} value of PMo-CoNiS is superior to the catalysts of CoNi LDH, CoNiS, Mo-CoNiS, and PW-CoNiS, and even surpassed that of commercial RuO_2/NF, which implies the fastest electron transfer between the interface of electrode and electrolyte. The CV of CoNi LDH, CoNiS, and Mo-CoNiS with different scan rates are shown in Fig. S12. For the samples of CoNiS and Mo-CoNiS, the value surpasses that of NiCo LDH (5.38 mF cm^{-2}), implying the enhanced number of active sites for OER by solvothermal reaction (Fig. 5(d)). Moreover, the measured C_{dl} of PMo-CoNiS has the highest value with 11.47 mF cm^{-2} as compared with other catalysts, suggesting the highest ECSA related to the more exposed active sites due to the amorphous/crystalline hybrid nanostructures created by P and Mo dual doping, and thereby remarkably improved electrocatalytic OER performance.

The long-term chronoamperometry (i–t) method was conducted to assess the OER durability of PMo-CoNiS in a 1 M KOH solution. It can be seen that after the 48-h test, the catalyst exhibited a mere 7.3% decline in current density, demonstrating its excellent OER stability (Fig. 5(f)). To garner deeper insights into the long-term durability of OER, various characterizations such as SEM, HRTEM, and XPS were conducted for post-PMo-CoNiS electrocatalysts. As shown in Fig. S13, the SEM image shows that the nanosheet morphology of P, Mo-CoNiS is almost unchanged after the OER stability test (48 h i–t). In the HRTEM image of post-PMo-CoNiS, there are lattice stripes with a characteristic spacing of 0. 283 nm assigned to the (311) plane of Co_3S_4 and abundant amorphous phase. Moreover, the generated thin amorphous phase with a thickness of 1–2 nm on the surface of the catalyst can be described as metal (oxy)hydroxides layer (Fig. S14), indicating that PMo-CoNiS has undergone the surface oxidation and electrochemical reconstruction during the continuous OER process. Meanwhile, the EDX element mapping image in Fig. S15 shows that Co, Ni, S, and Mo elements are uniformly distributed in the post-PMo-CoNiS after OER stability testing. The elemental analysis shows that the Co, Ni, S, and Mo element contents of the PMo-CoNiS after the OER stability test are 51.64 at%, 47.03 at%, 0.92 at%, and 0.51 at%, respectively, indicating the partial leaching of S and Mo. The P element cannot be detected due to trace doping. Furthermore, the XPS spectra of post-PMo-CoNiS are also characterized. Notably, as observed from the Co 2p and Ni 2p spectra in Fig. S16, the peaks at 781.0 eV and 855.5 eV emerged. It indicates the formation of high-valence states Co^{3+} and Ni^{3+} caused by the surface reconstruction of the Co_3S_4/Ni_3S_2 hybrid, which is attributed to NiOOH and CoOOH, respectively. These surface metal (oxy)hydroxide groups may function as active sites during the OER process [45]. In the high-resolution spectrum of the S 2p spectrum, the intensity of XPS peaks turns to weaken in comparison with the original one, indicating the lasting dissolution of S into electrolyte during OER. Meanwhile, the reduced intensity of Mo 3d peaks suggests the loss of Mo elements in PMo-CoNiS. This result agrees well with the reported sulfide/molybdenum-based OER electrocatalysts under alkaline conditions [46]. Besides, the small amount of P resided in PMo-CoNiS also disappeared for its leaching. In summary, the superior OER performance of PMo-CoNiS can be ascribed to its adjustable P and Mo doping, judiciously engineered amorphous/crystalline nanostructures, and unique hierarchical morphology.

3.2.2. HER performance and overall water splitting

Similarly, in the case of HER, PMo-CoNiS exhibits outstanding activity with the smallest overpotentials, which is superior to other samples of PMo_x-CoNiS (Fig. S17). Moreover, comparative evaluation using LSV PMo-CoNiS reveals that the PMo-CoNiS electrode also outperforms alternative electrodes such as CoNi LDH, CoNiS, Mo-CoNiS, and PW-CoNiS in HER activities (Fig. 6(a)). In detail, PMo-CoNiS achieves an overpotential of just 58 mV to deliver the current density of 10 mA cm^{-2}. In contrast, the CoNi LDH, CoNiS, Mo-CoNiS, and commercial Pt/C (20 wt%) catalyst possess overpotentials of 264, 196, 173, 154, and 38 mV, respectively, demonstrating that the synergistic effect of P and Mo species play an essential role in the enhanced HER activity. Moreover, the PMo-CoNiS electrode also shows better HER activity than PW-CoNiS. The over-

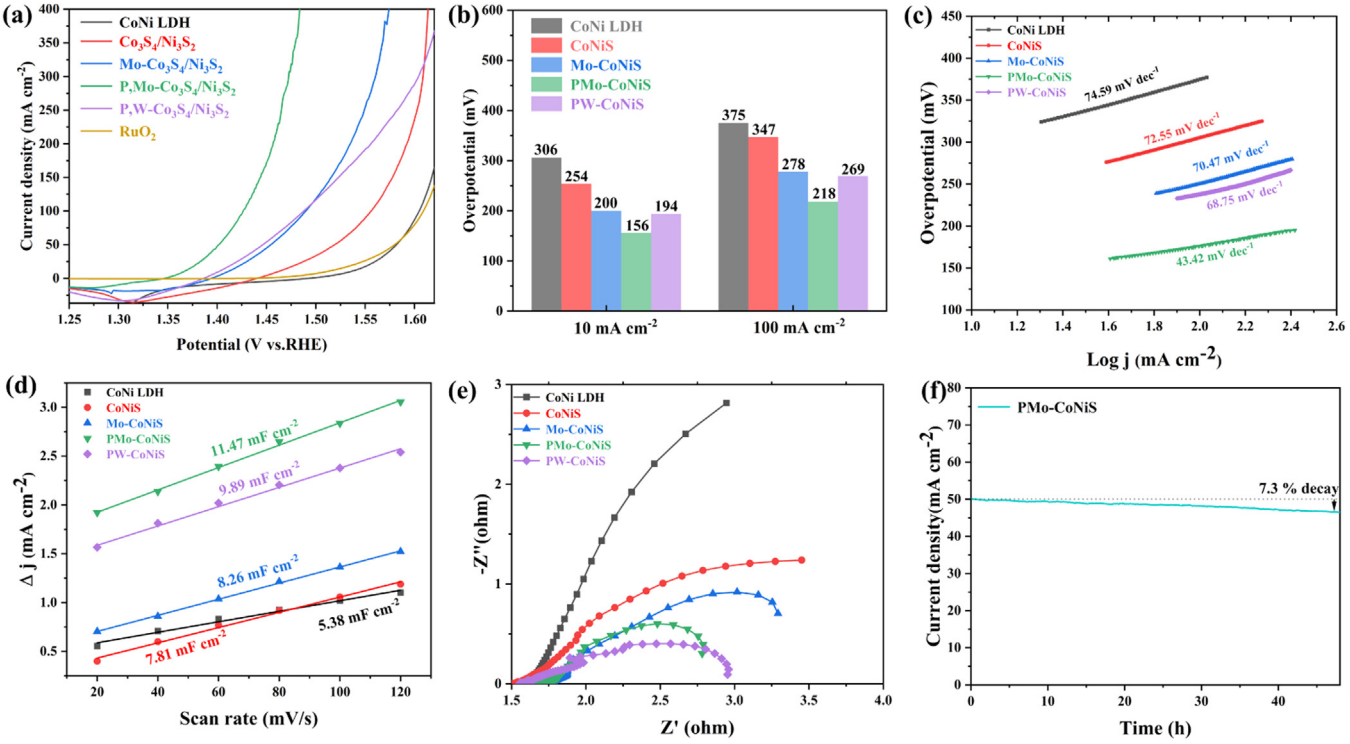

Fig. 5. Electrocatalytic OER performance. (a) The LSV polarization curves with iR compensation, (b) comparison of the current densities at 10, 100 mA cm^{-2} among different catalysts in 1 M KOH. (c) The corresponding Tafel slopes, (d) electrochemical double-layer capacitance, and (e) Nyquist plots of CoNi LDH, CoNiS, Mo-CoNiS, PW-CoNiS, and PMo-CoNiS catalysts in 1.0 M KOH. (f) The electrolyte chronopotentiometry curve of PMo-CoNiS recorded at the current density of 50 mA cm^{-2}.

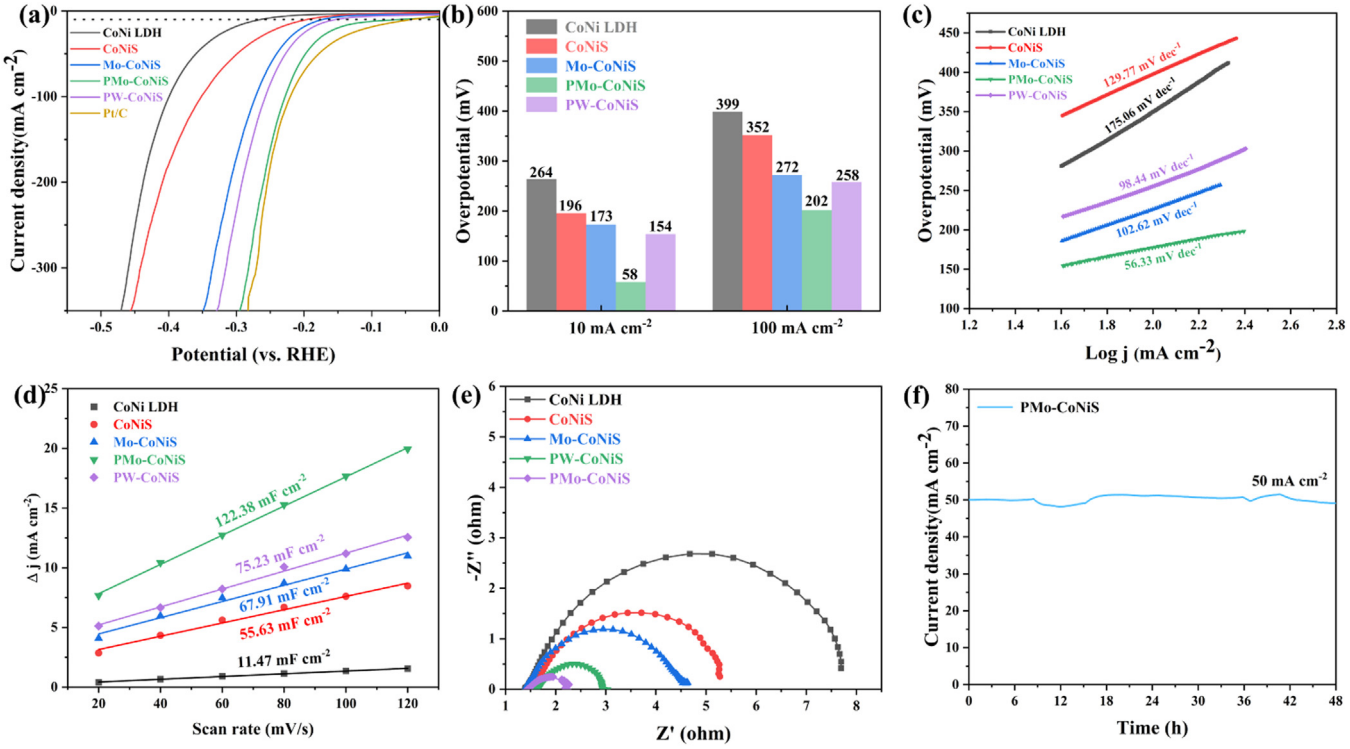

Fig. 6. Electrocatalytic HER performance. (a) The LSV polarization curves with iR compensation, (b) comparison of the current densities at 10, 100 mA cm^{-2} among different catalysts in 1 M KOH. (c) The corresponding Tafel slopes, (d) electrochemical double-layer capacitance, and (e) Nyquist plots of CoNi LDH, CoNiS, Mo-CoNiS, PW-CoNiS, and PMo-CoNiS catalysts in 1.0 M KOH. (f) The electrolyte chronopotentiometry curve of PMo-CoNiS recorded at the current density of 50 mA cm^{-2}.

potential of PMo-CoNiS (202 mV) is exceptionally superior to that of other as-fabricated catalysts when the current density achieves 100 mA cm^{-2} (Fig. 6(b)), further displaying the excellent HER activity of the PMo-CoNiS at a large current density. In addition, the outstanding activity of electrocatalytic PMo-CoNiS is superior to that of most recently reported sulfide-based HER electrocatalysts (Table S3). The Tafel slope was fitted to investigate the kinetic features of catalysts. PMo-CoNiS (56.33 mV dec^{-1}) has a smaller value than CoNi LDH (175.06 mV dec^{-1}), CoNiS (129.77 mV dec^{-1}), Mo-CoNiS (102.62 mV dec^{-1}), and PW-CoNiS (98.44 mV dec^{-1}) as shown in Fig. 6(c), and its HER follows the Volmer–Heyrovsky mechanism in the alkaline solution [47,48]. The better electrocatalytic activity and faster HER kinetics can be attributed to the constructed amorphous/crystalline heterostructures by rational doped P, Mo species. Moreover, the activity of the electrocatalyst is partly determined by the number of active sites. It can be seen that the C_{dl} value increased significantly after the sulfurization treatment, suggesting the enhanced number of active sites. In addition, the C_{dl} value of PMo-CoNiS is higher than that of PW-CoNiS, Mo-CoNiS, and CoNiS (Figs. 6(d) and S18). EIS measurements were employed to investigate the charge transfer kinetic characters to gain further insight into the HER process of these electrodes. It can be observed that PMo-CoNiS has a minor semicircle diameter among the tested electrodes, as shown in Fig. 6(e), which is lower than those of CoNi LDH, CoNiS, and Mo-CoNiS, implying that PMo-CoNiS undergoes the fastest charge transfer process during HER. Besides the superior electrocatalytic performance, long-term stability is another target to ensure that electrocatalysts can be employed in practical applications. The long-term chronoamperometry (i–t) method was conducted to assess the durability of PMo-CoNiS in a 1 M KOH solution. The current density of samples only slightly declined under the current density of 50 mA cm^{-2} after the 48-h test, verifying its excellent long-term stability (Fig. 6(f)). SEM and TEM characterizations post-HER testing showed that the hierarchical nanostructures of interwoven nanosheets on the micron sheets remained largely intact (Figs. S19–S21). In addition, XPS characterization of samples post-HER stability testing was conducted. Compared with the pristine PMo-CoNiS, very few changes in phase compositions and valence states occurred (Fig. S22). All these results indicate that the excellent structural stability, mass transfer properties, and mechanical stability of PMo-CoNiS during the HER process can be attributed to its unique nanostructures, and abundant heterogeneous interfaces.

Given the promising bifunctional electrocatalytic performance towards HER and OER, a typical two-electrode electrolytic system was used to further evaluate the overall water-splitting catalytic activity for accessible applications to water electrolysis, where PMo-CoNiS electrode was utilized as both the anode and cathode as illustrated in Fig. 7(a). The electrolyzer impressively required small cell voltages of 1.48 and 1.63 V to achieve the current density of 10 and 100 mA cm^{-2}, which outperform those of Mo-CoNiS||Mo-CoNiS (1.75, 1.84 V), CoNiS||CoNiS (1.93, 2.03 V) and Pt/C||RuO_2 (1.76, 1.88 V) as shown in Fig. 7(d). Fig. 7(c) exhibits a comprehensive evaluation of PMo-CoNiS activity towards overall water splitting in comparison with CoNiS, demonstrating the superiority of P, Mo dual doping. Utilizing solar energy as a sustainable and eco-friendly power source, commercial solar cells were integrated to energize the overall water splitting of PMo-CoNiS||PMo-CoNiS devices (Fig. 7(b)). Video S1 shows that this solar-powered H_2 production system can continuously release O_2 and H_2 bubbles at the voltage of 1.7 V, indicating that non-noble metal-based electrocatalysts fabricated by our strategy are feasible in practical

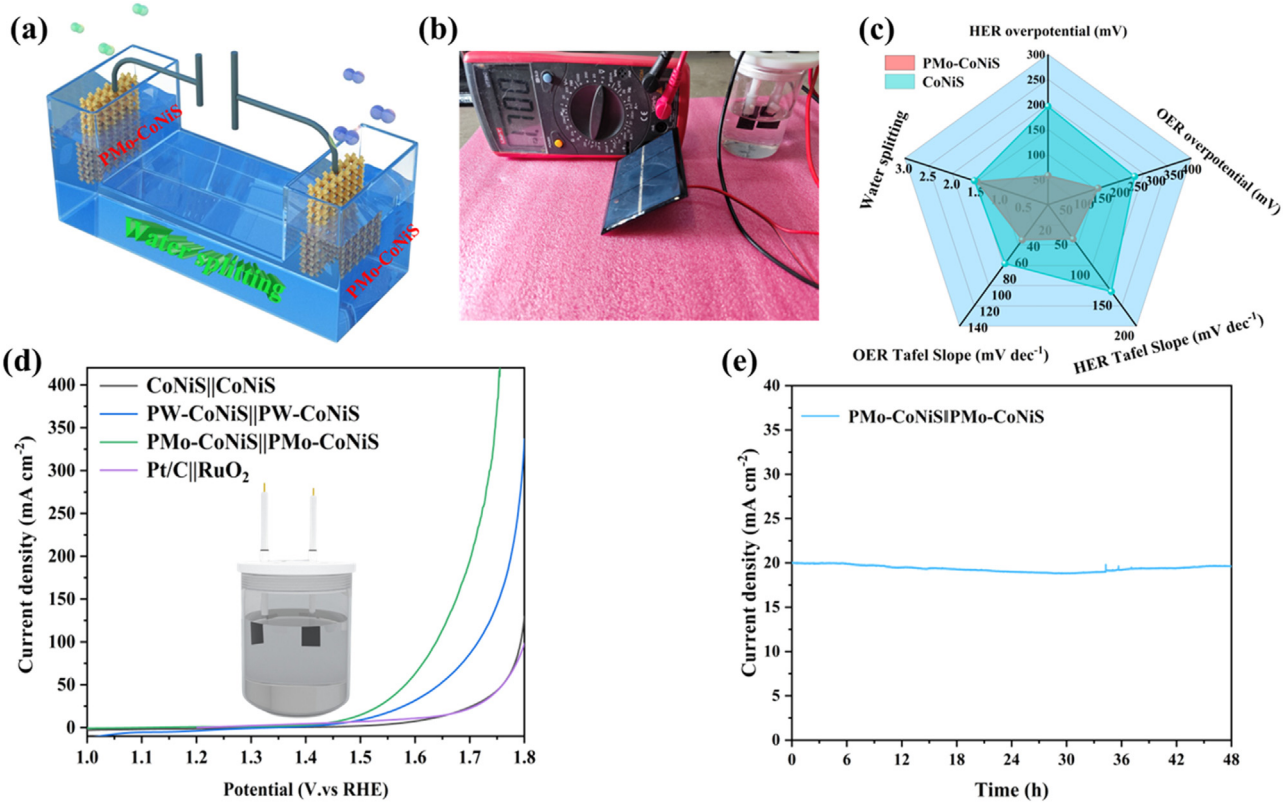

Fig. 7. (a) Schematic diagram of the electrolyzer using PMo-CoNiS as the cathode and anode, respectively. (b) The two-electrode water-splitting device powered by a solar cell with a voltage of 1.7 V. (c) Summary of the electrocatalytic performance of PMo-CoNiS (Overpotential of OER and HER at 10 mA cm^{-2}, the Tafel slope of OER and HER, and cell voltage for water splitting at 10 mA cm^{-2}). (d) Polarization curves conducted on a two-electrode configuration for overall water splitting in 1.0 M KOH. (e) The Chronoamperometric curve of PMo-CoNiS||PMo-CoNiS devices at 20 mA cm^{-2} for 48 h.

applications. Besides, the durability of the PMo-CoNiS||PMo-CoNiS was employed to conduct the long-term chronopotentiometry test. The PMo-CoNiS||PMo-CoNiS couple experienced a minor decay of only 3.9 % for operations at the current density of 20 mA cm^{-2} for 48 h in 1 M KOH, demonstrating its good stability for overall water splitting (Fig. 7(e)). These all indicate that PMo-CoNiS heterogeneous nanoarrays have great potential for application in water-splitting systems. Such impressive stability and performance of the catalyst PMo-CoNiS can be attributed to three key factors: (1) the unique hierarchical nanostructures composed of interconnected nanosheets facilitated rapid charge transport, promoting electrolyte penetration and bubble release, and strengthened the close contact between the active site and the reactants and mechanical stability [49]. (2) The abundant amorphous/crystalline heterointerfaces originated from dual-doping sulfides expand the electrochemically active surface area, expose more active sites, and enhance the conductivity. (3) The intense coupling effects from the constructed heterointerfaces between bimetallic sulfides efficiently modulate the electronic structures of electrocatalysts, thus optimizing the equilibrium adsorption of hydrogen (H*) and oxygen (*OH) intermediates. Therefore, our work reveals enhanced HER, OER, and water-splitting performance and stability of PMo-CoNiS, which opens up new horizons for designing and fabricating durable electrochemical energy conversion devices.

3.3. DFT and catalytic mechanism of PMo-CoNiS

To gain deep insight into the doping effect on improving the catalytic performance of the PMo-CoNiS at the atomic level, DFT calculations were carried out with the Vienna *Ab Initio* Simulation Package (VASP), as described in the Supporting information. The theoretical models of PMo-CoNiS are constructed in Fig. 8(a). According to the previous report, Co is regarded as the active center to explore the catalytic mechanism. It is worth noting that the Mo site is generally not considered the real active center for OER/HER in an alkaline solution due to its relatively low electrode potential and dissolution activation energy [50,51]. In theory, the catalytic behavior of the HER is heavily influenced by the Gibbs free energy of hydrogen bonding (ΔG_{H^*}). A $|\Delta G_{H^*}|$ value close to zero indicates exceptional activity, signaling an optimal strength for both H adsorption and desorption [52,53]. The free energy of intermediate H* adsorption (ΔG_{H^*}) for CoNiS, Mo-CoNiS, and PMo-CoNiS was calculated in Fig. 8(d), of which the ΔG_{H^*} value of PMo-CoNiS is 0.39 eV, significantly lower than those of Mo-CoNiS (0.65 eV) and CoNiS (1.23 eV), illuminating that the dual doping of P and Mo can enhance the binding with H intermediate and substantially increase the intrinsic HER activity. Moreover, the adsorption energies of H_2O molecules (ΔE_{H2O}) on the surfaces of CoNiS, Mo-CoNiS, and PMo-CoNiS models were computed, as they play a crucial role in an alkaline HER and water splitting (Fig. S23). Notably, neither excessively high nor low adsorption energy is favorable for the desorption or adsorption of ΔE_{H2O}, as it results in a higher energy barrier for the reaction [40,54]. PMo-CoNiS exhibits an optimal ΔE_{H2O} value of −0.143 eV compared to Mo-CoNiS (−0.146 eV) and CoNiS (−0.134 eV). This demonstrates an appropriate binding strength of H_2O molecules on the surface of PMo-CoNiS, facilitating the water adsorption process. Consequently, the optimized ΔG_{H^*} and more favorable H_2O adsorption processes collectively facilitate the high performance for HER, highlighting the advantages of PMo-CoNiS as an efficient catalyst.

Furthermore, DFT calculations were employed to elucidate the improved intrinsic OER activity of PMo-CoNiS through doping. Fig. 8(e) displays the OER pathways for both original and doped CoNiS under an external bias of 0 V, respectively, disclosing the Gibbs free energy of various oxygen-containing intermediates, including *OH, *O, and *OOH. It can be observed that the rate-determining step (RDS) of CoNiS is the third step (*O→*OOH), requiring a high overpotential of 0.857 V, which significantly impedes the OER process. After Mo doping, the overpotential is reduced to 0.832 V, indicating accelerated OER kinetics. Notably, the RDS shifts to the second step involving the reaction from *OH to *O for dual-doping PMo-CoNiS, and the required overpotential is substantially reduced to 0.543 eV. Based on the Gibbs free energy diagrams, the significant overpotentials result from the strong binding between the reaction intermediates and the sites. To explore the relationship between the electronic structure and the OER perfor-

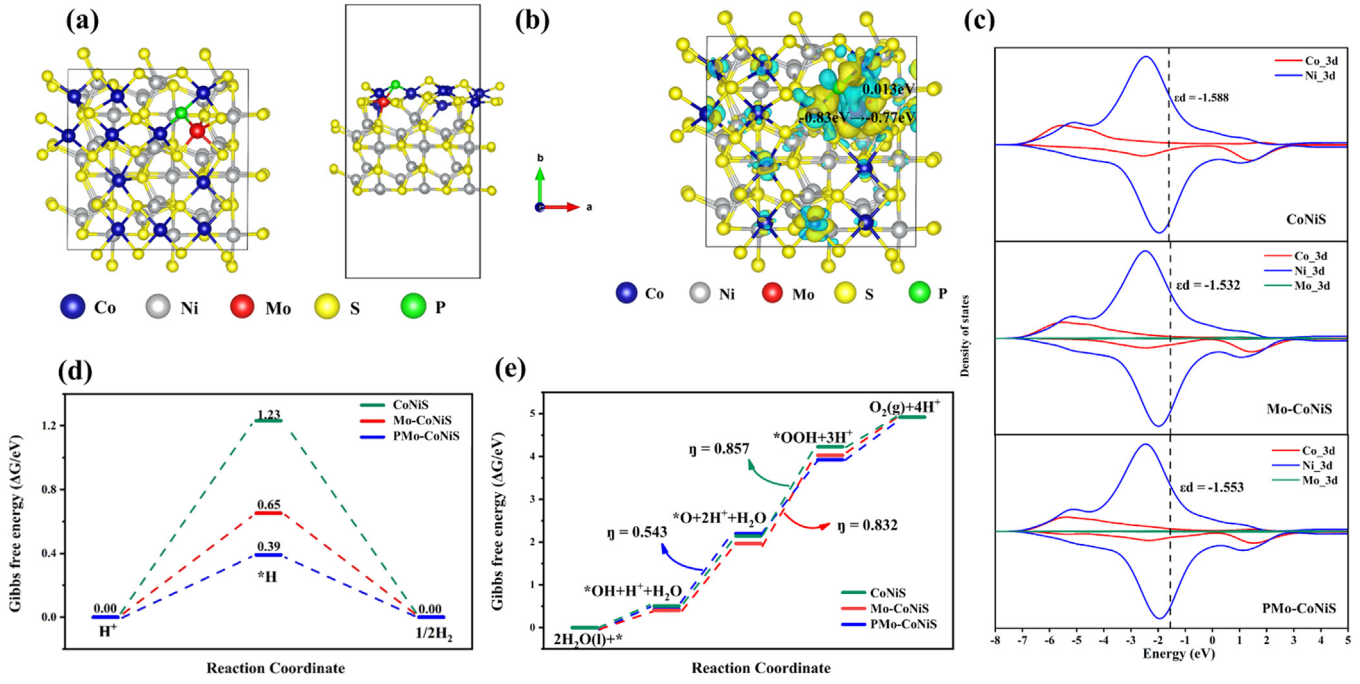

Fig. 8. (a) Top and side views of the PMo-CoNiS, (b) The Bader charge density difference and electron transference of PMo-CoNiS. (c) The total density of states (DOS) of CoNiS, Mo-CoNiS, and PMo-CoNiS. (d) Calculated free energy diagram of H adsorption for PMo-CoNiS, (e) Calculated free energy diagram of OER intermediates ($U = 0$).

mance of the catalyst after P, Mo dual doping, we also calculated the density of states (DOS) of CoNiS, Mo-CoNiS, and PMo-CoNiS. The d-band center value partly reflects the correlation between active sites' catalytic activity and the intermediate species' bond strength. According to the d-band theory, a d-band center value close to the Fermi level usually indicates a strong binding affinity between the active sites and the adsorbed species, facilitating the adsorption of water molecules and intermediate reactive species [43]. Conversely, a d-band center value farther from the Fermi level would lead to a weaker binding affinity, facilitating rapid hydrogen and oxygen desorption. In Fig. 8(c), the PMo-CoNiS sample exhibits an appropriate d-band center value (−1.55 eV), compared to Mo-CoNiS (−1.53 eV) and CoNiS (−1.59 eV). In addition, we performed differential charge density calculations to analyze the electronic reconstruction. As shown in Fig. 8(b), yellow stands for accumulated charge, and blue signifies lost charge. It is evident from the analysis that the electrons lost 0.83 eV in Mo-CoNiS compared to undoped CoNiS, indicating a high Co charge loss after Mo doping. However, for PMo-CoNiS, the Co atoms at the active sites show a smaller charge loss of 0.77 eV, and the S sites accumulated 0.013 eV. These charge accumulation and depletion create a built-in electric field that promotes the transfer of charges at the interface. Such charge transfer of metal atoms at the interface optimizes the interaction between the metal atoms and the reaction intermediates. The result indicates that doping of P and Mo can cause a redistribution of the electronic structure, thereby enhancing the electron environment for electrocatalytic reactions [49]. Thus, dual-doping heterogeneous CoNiS can efficiently modulate the charge transfer between the catalyst and the intermediate, altering the adsorption strength and the Gibbs free energy of the reaction, and ultimately strengthening both the OER and HER catalytic activity.

4. Conclusions

In conclusion, we have successfully fabricated novel P and Mo dual-doped CoNiS nanosheet arrays through a facile solvothermal treatment, demonstrating excellent catalytic activity for overall water splitting. The amorphous/crystalline hybrid nanostructures, by precise dual doping of P and Mo, can adjust the electronic structure and optimize the adsorption/desorption of H*, OH*, and water molecules, enhancing the intrinsic activity toward HER and OER. As a result, ultralow overpotentials of only 156 and 58 mV are required to achieve a current density of 10 mA cm^{-2} for OER and HER, and the electrocatalyst PMo-CoNiS also exhibited low Tafel slope and maintained robust stability for 48 h under a large current density of 50 mA cm^{-2} in alkaline media. Furthermore, the assembled electrolyte cell for overall water splitting only needed 1.48 V to achieve the current density of 10 mA cm^{-2}. This work showcases a low-cost catalyst with excellent intrinsic activity, providing a new approach for designing high-performance bifunctional electrodes in a wide range of electrocatalytic fields.

Declaration of competing interest

The authors declare that they have no known competing financial interests or personal relationships that could have appeared to influence the work reported in this paper.

Acknowledgments

The authors greatly acknowledge the financial support of the National Natural Science Foundation of China (22078233). Thanks to eceshi (www.eceshi.com) for conducting the XPS analysis.

Supplementary materials

Supplementary material associated with this article can be found, in the online version, at doi:10.1016/j.jmst.2024.02.082.

References

[1] H.-M. Zhang, L. Zuo, Y. Gao, J. Guo, C. Zhu, J. Xu, J. Sun, J. Mater. Sci. Technol. 173 (2024) 1–10.
[2] G. Li, F. Yang, S. Che, H. Liu, N. Chen, J. Qian, C. Yu, B. Jiang, M. Liu, Y. Li, J. Mater. Sci. Technol. 166 (2023) 58–66.
[3] C.-L. Huang, Y.-G. Lin, C.-L. Chiang, C.-K. Peng, D.S. Raja, C.-T. Hsieh, Y.-A. Chen, S.-Q. Chang, Y.-X. Yeh, S.-Y. Lu, Appl. Catal. B-Environ. 320 (2023) 122016.
[4] Q. Niu, M. Yang, D. Luan, N.W. Li, L. Yu, X.W. Lou, Angew. Chem.-Int. Edit. 61 (2022) e202213049.
[5] Y. Sun, K. Xu, Z. Wei, H. Li, T. Zhang, X. Li, W. Cai, J. Ma, H.J. Fan, Y. Li, Adv. Mater. 30 (2018) 1802121.
[6] C. Xu, X. Yang, K. Feng, M. Zhang, L. Yang, S. Yin, A.C.S. Appl, Energ. Mater. 6 (2023) 1404–1412.
[7] J.-S. Li, Y. Wang, C.-H. Liu, S.-L. Li, Y.-G. Wang, L.-Z. Dong, Z.-H. Dai, Y.-F. Li, Y.-Q. Lan, Nat. Commun. 7 (2016) 11204.
[8] C. Chen, L. Jin, L. Hu, T. Zhang, J. He, P. Gu, Q. Xu, J. Lu, J. Colloid Interface Sci. 628 (2022) 1008–1018.
[9] J. Zhang, S. Huang, P. Ning, P. Xin, Z. Chen, Q. Wang, K. Uvdal, Z. Hu, Nano Res. 15 (2022) 1916–1925.
[10] T. Zhao, D. Zhong, L. Tian, G. Hao, G. Liu, J. Li, Q. Zhao, J. Colloid Interface Sci. 634 (2023) 630–641.
[11] X.F. Lu, S.L. Zhang, W.L. Sim, S. Gao, X.W. Lou, Angew. Chem.-Int. Edit. 133 (2021) 23067–23073.
[12] Y. Feng, X. Wang, J. Huang, P. Dong, J. Ji, J. Li, L. Cao, L. Feng, P. Jin, C. Wang, Chem. Eng. J. 390 (2020) 124525.
[13] Z. Wang, W. Liu, Y. Hu, M. Guan, L. Xu, H. Li, J. Bao, H. Li, Appl. Catal. B-Environ. 272 (2020) 118959.
[14] J. Zhang, T. Wang, D. Pohl, B. Rellinghaus, R. Dong, S. Liu, X. Zhuang, X. Feng, Angew. Chem.-Int. Edit. 128 (2016) 6814–6819.
[15] Y. Wu, G.D. Li, Y. Liu, L. Yang, X. Lian, T. Asefa, X. Zou, Adv. Funct. Mater. 26 (2016) 4839–4847.
[16] Q. Wang, H. Xu, X. Qian, G. He, H. Chen, Appl. Catal. B-Environ. 322 (2023) 122104.
[17] S. Tang, X. Wang, Y. Zhang, M. Courté, H.J. Fan, D. Fichou, Nanoscale 11 (2019) 2202–2210.
[18] Q. Xiong, Y. Wang, P.F. Liu, L.R. Zheng, G. Wang, H.G. Yang, P.K. Wong, H. Zhang, H. Zhao, Adv. Mater. 30 (2018) 1801450.
[19] D.T. Tran, S. Prabhakaran, D.H. Kim, N. Hameed, H. Wang, N.H. Kim, J.H. Lee, Nano Energy 88 (2021) 106277.
[20] S. Ni, H. Qu, Z. Xu, X. Zhu, H. Xing, L. Wang, J. Yu, H. Liu, C. Chen, L. Yang, Appl. Catal. B-Environ. 299 (2021) 120638.
[21] K. Wang, Y. Guo, Z. Chen, D. Wu, S. Zhang, B. Yang, J. Zhang, InfoMat 4 (2022) e12251.
[22] F. Du, L. Shi, Y. Zhang, T. Li, J. Wang, G. Wen, A. Alsaedi, T. Hayat, Y. Zhou, Z. Zou, Appl. Catal. B-Environ. 253 (2019) 246–252.
[23] Y. Zhang, F. Gao, D. Wang, Z. Li, X. Wang, C. Wang, K. Zhang, Y. Du, Coord. Chem. Rev. 475 (2023) 214916.
[24] J. Ding, T. Fan, K. Shen, Y. Li, Appl. Catal. B-Environ. 292 (2021) 120174.
[25] Z. Dong, F. Lin, Y. Yao, L. Jiao, Adv. Energy Mater. 9 (2019) 1902703.
[26] J. Xu, X. Kong, Small Methods 6 (2022) 2101432.
[27] K. Zheng, J. Ren, X. Li, G. Li, L. Jiao, C. Xu, Chem. Eng. J. 441 (2022) 136031.
[28] X. Yang, F. Peng, L. Zhang, X. Wang, S. Liu, W. Yang, L. Zhang, N. Yang, Chem. Eng. J. 449 (2022) 137901.
[29] G. Zhou, M. Li, Y. Li, H. Dong, D. Sun, X. Liu, L. Xu, Z. Tian, Y. Tang, Adv. Funct. Mater. 30 (2020) 1905252.
[30] B. Fei, Z. Chen, J. Liu, H. Xu, X. Yan, H. Qing, M. Chen, R. Wu, Adv. Energy Mater. 10 (2020) 2001963.
[31] J. Wang, J. Hu, C. Liang, L. Chang, Y. Du, X. Han, J. Sun, P. Xu, Chem. Eng. J. 446 (2022) 137094.
[32] W. Peng, A. Deshmukh, N. Chen, Z. Lv, S. Zhao, J. Li, B. Yan, X. Gao, L. Shang, Y. Gong, L. Wu, M. Chen, T. Zhang, H. Gou, ACS Catal. 12 (2022) 3743–3751.
[33] L. Zhao, C. Gong, X. Chen, X. He, H. Chen, X. Du, D. Wang, W. Fang, H. Zhang, W. Li, Appl. Surf. Sci. 623 (2023) 157030.
[34] Y.-T. Xu, Z.-M. Ye, J.-W. Ye, L.-M. Cao, R.-K. Huang, J.-X. Wu, D.-D. Zhou, X.-F. Zhang, C.-T. He, J.-P. Zhang, X.-M. Chen, Angew. Chem.-Int. Edit. 58 (2019) 139–143.
[35] Y. Zhou, J. Zhang, H. Ren, Y. Pan, Y. Yan, F. Sun, X. Wang, S. Wang, J. Zhang, Appl. Catal. B-Environ. 268 (2020) 118467.
[36] Z. Cai, X. Bu, P. Wang, W. Su, R. Wei, J.C. Ho, J. Yang, X. Wang, J. Mater. Chem. A 7 (2019) 21722–21729.
[37] X. Luo, P. Ji, P. Wang, R. Cheng, D. Chen, C. Lin, J. Zhang, J. He, Z. Shi, N. Li, S. Xiao, S. Mu, Adv. Energy Mater. 10 (2020) 1903891.
[38] B. Yuan, C. Li, L. Guan, K. Li, Y. Lin, J. Power Sources 451 (2020) 227295.
[39] T. Wang, L. Wu, X. Xu, Y. Sun, Y. Wang, W. Zhong, Y. Du, Sci. Rep. 7 (2017) 11891.
[40] H. Su, S. Song, S. Li, Y. Gao, L. Ge, W. Song, T. Ma, J. Liu, Appl. Catal. B-Environ. 293 (2021) 120225.
[41] V.H. Hoa, D.T. Tran, D.C. Nguyen, D.H. Kim, N.H. Kim, J.H. Lee, Adv. Funct. Mater. 30 (2020) 2002533.

[42] Q. Wu, A. Dong, C. Yang, L. Ye, L. Zhao, Q. Jiang, Chem. Eng. J. 413 (2021) 127482.
[43] H. Wang, J. Xu, Q. Zhang, S. Hu, W. Zhou, H. Liu, X. Wang, Adv. Funct. Mater. 32 (2022) 2112362.
[44] Y. Li, Z. Mao, Q. Wang, D. Li, R. Wang, B. He, Y. Gong, H. Wang, Chem. Eng. J. 390 (2020) 124556.
[45] X. Zhou, Y. Mo, F. Yu, L. Liao, X. Yong, F. Zhang, D. Li, Q. Zhou, T. Sheng, H. Zhou, Adv. Funct. Mater. 33 (2023) 2209465.
[46] X. Wang, Y. He, X. Han, J. Zhao, L. Li, J. Zhang, C. Zhong, Y. Deng, W. Hu, Nano Res. 15 (2022) 1246–1253.
[47] V.H. Hoa, D.T. Tran, H.T. Le, N.H. Kim, J.H. Lee, Appl. Catal. B-Environ. 253 (2019) 235–245.
[48] Y. Zhang, Q. Shao, S. Long, X. Huang, Nano Energy 45 (2018) 448–455.
[49] Q. Quan, Y. Zhang, F. Wang, X. Bu, W. Wang, Y. Meng, P. Xie, D. Chen, W. Wang, D. Li, C. Liu, S. Yip, J.C. Ho, Nano Energy 101 (2022) 107566.
[50] J. Zhu, R. Lu, F. Xia, P. Wang, D. Chen, L. Chen, J. Yu, Y. Zhao, J. Wu, S. Mu, Nano Energy 110 (2023) 108349.
[51] D. Li, Y. Qin, J. Liu, H. Zhao, Z. Sun, G. Chen, D.-Y. Wu, Y. Su, S. Ding, C. Xiao, Adv. Funct. Mater. 32 (2022) 2107056.
[52] D. Chen, Z. Pu, P. Wang, R. Lu, W. Zeng, D. Wu, Y. Yao, J. Zhu, J. Yu, P. Ji, ACS Catal. 12 (2022) 2623–2631.
[53] Y. Guo, B. Hou, X. Cui, X. Liu, X. Tong, N. Yang, Adv. Energy Mater. 12 (2022) 2201548.
[54] J.K. Nørskov, T. Bligaard, A. Logadottir, J. Kitchin, J.G. Chen, S. Pandelov, U. Stimming, J. Electrochem. Soc. 152 (2005) J23.